Letter | Editors' Suggestion

Element- and atomic-layer-resolved detection of surface magnetism via x-ray-excited tunneling

Sineth Premarathna,[1] Kyaw Zin Latt,[1] Nozomi Shirato,[2] Sarah Wieghold,[3] Daniel Rosenmann,[2] Alex Taekyung Lee,[4] Anh T. Ngo,[4] Volker Rose,[3] and Saw Wai Hla[1,5,*]

[1]*Nanoscale and Quantum Phenomena Institute, Physics & Astronomy Department, Ohio University, Athens, Ohio 45701, USA*
[2]*Center for Nanoscale Materials, Argonne National Laboratory, Lemont, Illinois 60439, USA*
[3]*Advanced Photon Source, Argonne National Laboratory, 9700 South Cass Avenue, Lemont, Illinois 60439, USA*
[4]*Department of Chemical Engineering, University of Illinois at Chicago, Chicago, Illinois 60608, USA*
[5]*Materials Science Division, Argonne National Laboratory, Lemont, Illinois 60439, USA*

(Received 31 July 2025; accepted 5 August 2026; published 1 September 2026)

Element-specific magnetism at the atomic scale is important in low-dimensional materials such as thin magnetic films and quantum dots, where interfacial and surface effects can give rise to novel behavior. However, probing magnetism specific to the topmost atomic layer remains a key experimental challenge. Here, we introduce a synchrotron x-ray scanning tunneling spectroscopy approach that enables detection and quantification of surface magnetism via x-ray-excited electron tunneling. By illuminating a scanning tunneling microscope tip-sample junction with circularly polarized x-rays tuned to the Ni $L_{2,3}$ absorption edges, ensemble-averaged and surface atomic-layer x-ray magnetic circular dichroism are simultaneously measured on a ∼2.5-monolayer-thick Ni film grown on a Cu(111) surface. Measurements are performed at substrate temperatures of 90 and 22 K. The results reveal enhanced orbital and spin magnetic moments in the outermost atomic layer as compared to the ensemble-averaged moments of the thin Ni film at both temperatures. This work establishes an experimental method for quantitative, element-specific magnetometry with atomic-layer sensitivity using x-rays.

DOI: 10.1103/2fdk-tmsx

Low-dimensional magnetic systems can exhibit exotic properties different from those of their bulk counterparts due to reduced symmetry, modified electronic hybridization, and interfacial coupling to substrates [1,2]. These effects can give rise to emerging magnetic phenomena, including skyrmions [3] and chiral spintronic structures [4]. They also play a crucial role in nanoscale magnetic materials such as nanoparticles and quantum dots and are vital for many applications, including spintronics, medicine, and sensors [5–7].

X-ray absorption spectroscopy (XAS), along with x-ray magnetic circular dichroism (XMCD) [8–10], and the surface magneto-optic Kerr (SMOKE) effect [11], have been used extensively to investigate magnetic properties at the few-monolayer limit [12–14]. The XMCD effect arises from the difference in absorption between left- and right-circularly polarized x-rays in magnetic materials. Through spin-orbit coupling, the helicity of incident photons determines the angular momentum transferred to excited electrons, thereby generating spin-polarized electronic excitations. In materials with an imbalance between spin-up and spin-down states, such as 3*d* transition metals, this leads to a measurable dichroic signal proportional to the magnetic moment. Several theoretical studies have predicted enhanced spin and orbital magnetic moments due to the narrowing of the *d* orbitals and lowering of symmetry at the surface atomic layer [15–17]. However, because the incident x-ray beam penetrates several atomic layers [18], it is challenging to study magnetic properties specific to the topmost atomic layer. Moreover, the spatial resolution in standard XMCD or SMOKE measurements is limited by the beam size. Therefore, atomic-scale magnetism has primarily been determined using spin-polarized scanning tunneling microscopy (SP-STM). SP-STM uses a magnetized tip to detect magnetic signals in materials at the atomic scale via magnetoresistive tunneling [19–21]. However, unlike x-rays, SP-STM relies on tunneling electrons near the Fermi level, and therefore elemental specificity is limited. Here, we demonstrate the detection of magnetism in the top-surface atomic layer of a Ni thin film grown on a Cu(111) substrate using x-ray-excited tunneling and explain the underlying detection mechanism.

To achieve elemental sensitivity with atomic-scale spatial resolution, synchrotron x-ray scanning tunneling microscopy (SX-STM) has been developed [22–27]. In SX-STM, the tip-sample junction is illuminated by monochromatic x-rays. Using a topographic filter, the conventional tunneling current is separated from the x-ray-excited tunneling contribution. This enables elemental and chemical identification at the one-atom limit [22]. In our setup, the sample current (I_S) and the tip current (I_T) are measured simultaneously using separate lock-in amplifiers [(Fig. 1(a)] [28]. The sample current arises from photoemitted electrons escaping from the entire x-ray-illuminated region and is analogous to total electron yield (TEY) detection in conventional XAS [22]. The tip current can be in two different regimes: far-field and tunneling. In the far-field configuration [23], the tip is positioned outside the tunneling distance, i.e., a few nanometers or more above the surface, and tunneling does not occur. The detected current signal at the tip then consists predominantly of photoelectrons emitted from the sample.

*Contact author: hla@ohio.edu

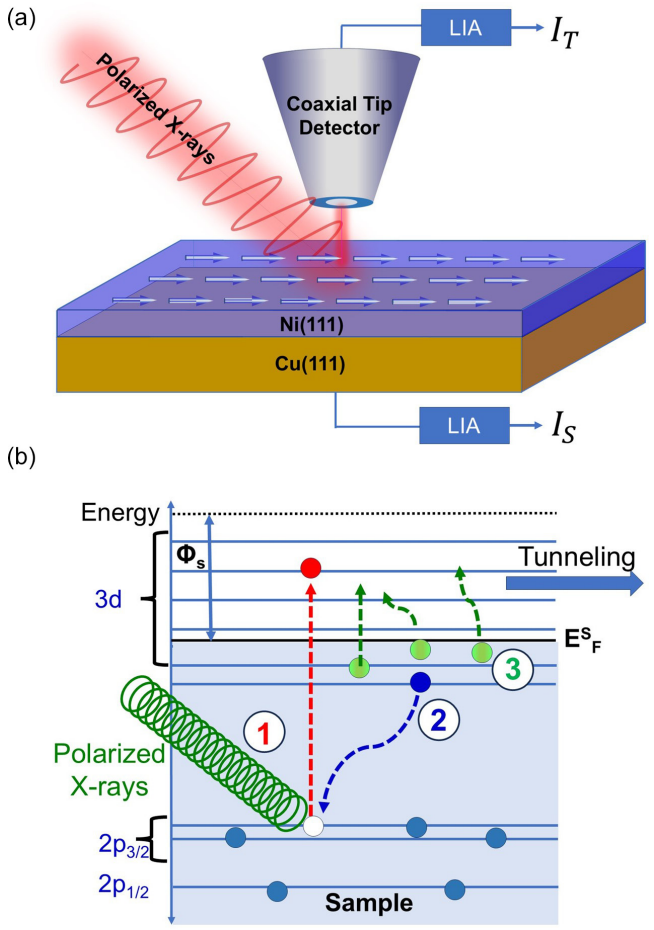

FIG. 1. (a) SX-STM experimental setup. A circularly polarized x-ray beam illuminates the tip-sample junction. Separate lock-in amplifiers (LIAs) are used to detect the sample (I_S) and tip (I_T) currents. (b) X-rays excite photoelectrons. The photoexcitation process leaves a vacancy (1), which is then filled by an electron from a higher orbital (2). An avalanche of Auger and secondary electrons (3) is produced; these electrons can fill unoccupied states and then tunnel to the tip.

In contrast, x-ray-excited tunneling (XET) occurs in the tunneling regime, where the tip is positioned ∼0.5 nm above the surface. The tip current in the tunneling regime originates from the tunneling of x-ray-excited electrons from the sample to the tip [(Fig. 1(b)]. Because tunneling current depends exponentially on tip-sample separation, this channel is extremely sensitive to the local atomic environment directly beneath the tip, as in scanning tunneling microscopy, and provides intrinsic atomic-scale sensitivity, even down to just one atom if the atom is isolated [22,29]. The contribution of nonlocal photoelectrons, i.e., photoejected electrons, to the x-ray-excited tunneling current signal is strongly suppressed when operating at tunneling distances [22,23,26,28]. This is because the coaxial tip geometry prevents photoelectrons emitted at large angles from striking the sidewalls of the tip and contributing to the far-field current. Moreover, the exposed tip apex is positioned in close proximity to the surface (∼0.5 nm), which strongly limits photoelectrons from more distant regions reaching the tip. Simultaneous TEY and XET measurements enable a direct comparison between the ensemble-averaged magnetism of the film and the atomic-scale local magnetism of the same sample, and it is greatly advantageous.

XET involves two sequential processes: core-level photoexcitation and electron tunneling. When the incident photon energy is tuned to a core-level resonance, such as the Ni $L_{2,3}$ edges, a core electron is excited, creating a core hole. The subsequent relaxation process produces secondary and Auger electrons [Fig. 1(b)]. A fraction of these electrons occupies states between the Fermi level and the vacuum level. These electrons can then tunnel into the STM tip, generating a measurable current. Because the initial excitation probability depends on photon helicity and on the projection of the sample magnetization vector onto the x-ray beam propagation vector, the resulting tunneling current carries XMCD contrast.

For the experiments, we used a Ni thin film grown on Cu(111), a well-studied model system suitable for this demonstration. For sample preparation, a Cu(111) single crystal was cleaned by repeated cycles of Ar+ ion sputtering and subsequently annealed to 600 K under ultrahigh vacuum (UHV). The Cu(111) substrate was cooled to 79 K before Ni deposition to prevent Cu interdiffusion into Ni [30]. Approximately 2.5 monolayers (MLs) coverage of Ni were deposited by thermal evaporation. Next, the sample was premagnetized by applying an in-plane external magnetic field in UHV for 15 s using an AlNiCo permanent magnet mounted near the sample stage. No external magnetic field was applied during the measurement; therefore, the measured magnetic state was remanent. Ni on Cu(111) exhibits magnetism even below 2 ML, with Ni spins preferentially aligning along the in-plane magnetic easy axis up to several monolayers [31] and has a critical temperature T_C above 150 K [32]. Figures 2(a) and 2(b) present an STM image and corresponding height profile of the Ni grown on the Cu(111) surface for this experiment. STM images reveal that multiple single-step islands coalesce to form the Ni layer.

The synchrotron experiments were performed at the XTIP beamline of the Center for Nanoscale Materials and the Advanced Photon Source at Argonne National Laboratory [33]. Left- and right-circularly polarized x-ray beams with a size of ∼10 μm × 10 μm were illuminated onto the tip-sample junction [Fig. 1(a)] at ∼30° relative to the surface plane after passing through an x-ray beam chopper operating at 590 Hz. XMCD measurements were performed in the tunneling regime, with the tip positioned ∼5 Å above the sample surface at a −1 V tunneling bias and a fixed tunneling current of 100 pA. The x-ray chopper modulated the x-rays between "on" and "off" states. During the x-ray-off period, the tunneling feedback loop maintained the tip height using the parameters described above. During the x-ray-on period, the STM feedback was inactive, and the tip remained stationary at the set point above the surface. The additional tunneling current induced by x-ray excitation during this period was then measured using a lock-in amplifier. The x-ray-induced current originates from primary, secondary, and Auger electrons generated during core-level x-ray excitation events [see Fig. 1(b)]. These electrons populate initially unoccupied states of the sample and subsequently tunnel to the detector tip. Because the conventional tunneling current associated with the −1 V bias is rejected by lock-in detection, the measured signal

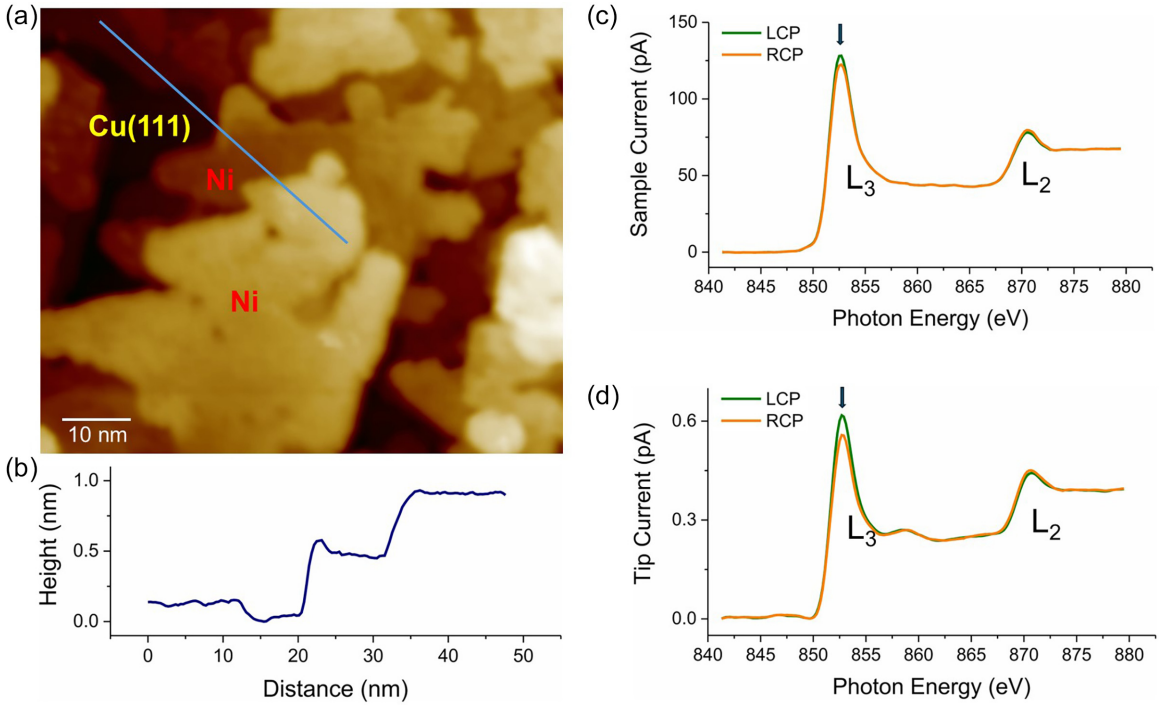

FIG. 2. (a) STM image of a Ni film grown on Cu(111) at a substrate temperature of 79 K [$V_T = 0.5$ V, $I_T = 0.1$ nA]. (b) Height profile across the line indicated in (a). (c) STM-XAS spectra of the sample channel (TEY mode) showing Ni $L_{2,3}$ edge signals measured with left- and right-circularly polarized (LCP, RCP) x-rays. (d) Simultaneously measured STM-XAS signals produced by XET in the tip channel. Arrows in (c), (d) indicate L_3 edge peaks.

predominantly reflects the tunneling current of x-ray-excited electrons that fill the unoccupied local density of states of Ni.

The x-ray absorption spectra are measured at substrate temperatures of 90 and 22 K, respectively. The data acquisition time for a complete spectrum is ∼3 min, and each recorded spectrum is an average of 40 spectra. Considering the photon flux of 1.94×10^{11} photons/s at 885 eV, the x-ray beam delivered only ∼27.5 μW of power to the sample; this corresponds to a power density of 27.5 mW/cm^2 for our x-ray beam size. The measured thermal drift at 90 K with the x-ray beam illuminating the sample is 0.65 nm/h. This corresponds to <1 Å thermal drift over a spectroscopic measurement time of 3 min. At 22 K, the thermal drift is 0.14 nm/h, corresponding to <0.1 Å over the spectroscopic measurement time. The low thermal drift of the system is achieved by maintaining both the tip and the sample at the same temperature.

Figure 2(c) presents average x-ray absorption spectroscopy (XAS) data measured in TEY mode in the sample channel at 90 K. Figure 2(d) shows the simultaneously measured STM-XAS spectra in XET mode at the tip channel. Both spectra show that the left-circularly polarized (LCP) x-ray signal (green) is higher than the right-circularly polarized (RCP) signal (orange) at the Ni L_3 edge at 852.7 eV [Figs. 2(c) and 2(d)]. The magnetization of Ni is evident in both spectra: the LCP is higher at the Ni L_3 edge, while the sign is reversed at the Ni L_2 edge at ∼870.5 eV, as expected. Here, the L_3 peak is generated by Ni $2p_{3/2} \rightarrow 3d$ transition, while the L_2 peak originates from the Ni $2p_{1/2} \rightarrow 3d$ transition.

Figure 2(d) clearly demonstrates that the local magnetic signature can be detected in the tunneling regime using the XET process. The detector tips used here are formed from PtIr or W wires coated with an insulating SiO_2 film and covered with an outer Au layer to prevent charging [22,23,28]. Therefore, the magnetic sensitivity in XET mode here does not arise from spin filtering at the tip, as in SPSTM. Instead, the XMCD contrast originates from the helicity-dependent core-level excitation probability, which leads to different numbers of excited electrons and, consequently, different tunneling currents for opposite photon helicities. Thus the intensity difference between the LCP and RCP signals in the XET mode is a direct consequence of the initial preferential photoexcitation process. Remarkably, comparison of the L_3-edge XAS spectra [Figs. 2(c) and 2(d), and 3(a) and 3(b)] clearly reveals that the difference between the LCP and RCP signals is significantly enhanced in XET relative to the TEY mode.

The XMCD sum rules relate dichroism and the total absorption to the ground-state orbital (m_L) and spin (m_S) magnetic moment of the sample [34–36], and they can be approximated as follows:

$$m_l = \frac{-4Qn_h}{3R}, \tag{1}$$

$$m_s = \frac{(4Q - 6P)n_h}{R}. \tag{2}$$

The quantities P and Q are extracted from the measured XMCD spectrum [37], where P is the cumulative integral after the L_3 edge, and Q is the cumulative integral after the L_2 edge in the XMCD plot [Figs. 3(c) and 3(d)]. The quantity R is extracted from the sum of the LCP and RCP signals and their cumulative integral after the L_2 edge [Figs. 3(e) and 3(f)], while n_h is the number of holes in the $3d$ valence band of Ni. In XMCD, the measured magnetic signal is proportional

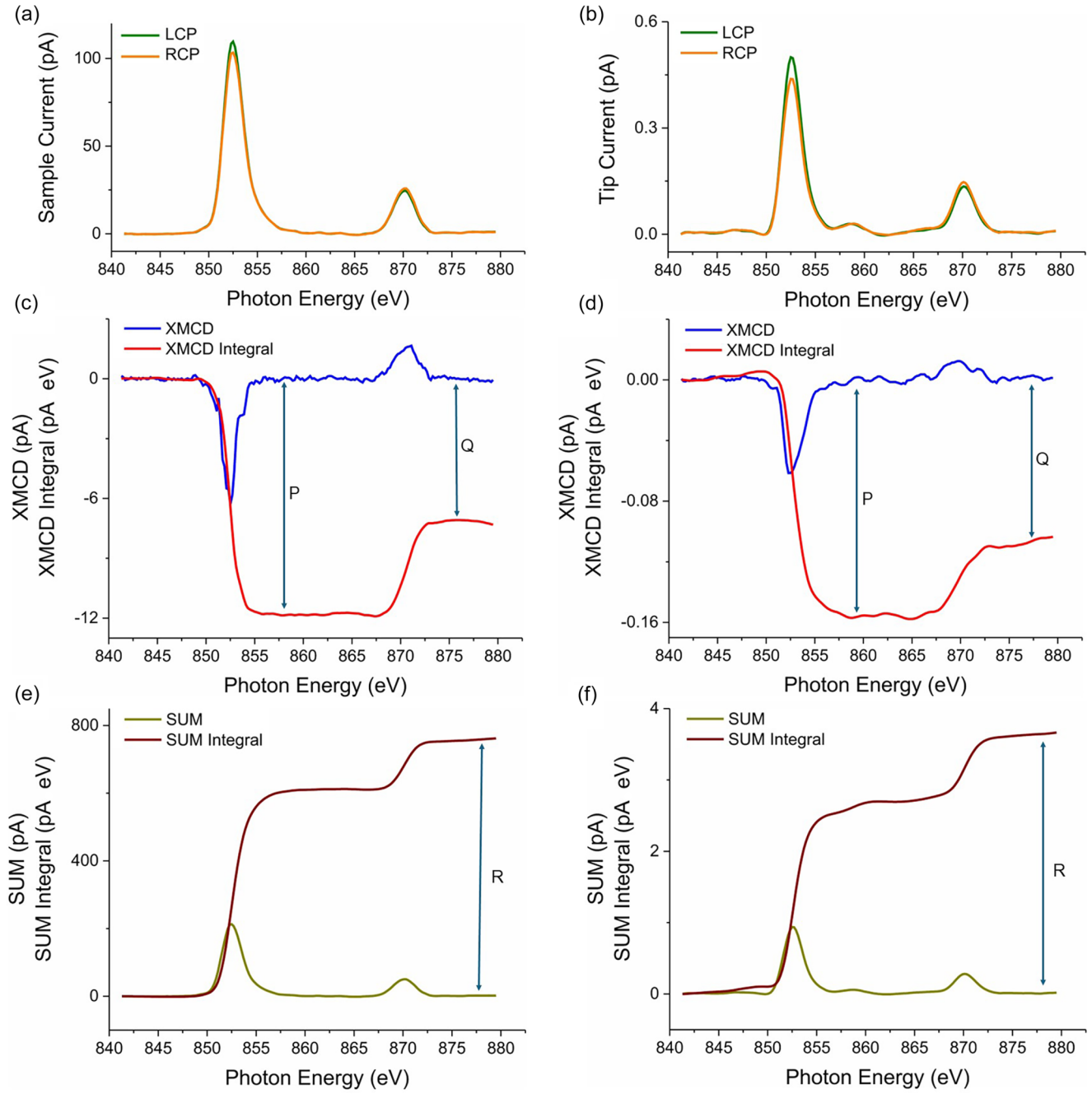

FIG. 3. (a) TEY-mode XAS spectra (sample channel) and (b) STM-XAS spectra in the XET regime measured at 90 K after L_3 and L_2 edge-jump background subtraction. (c), (d) XMCD and cumulative XMCD integral plots corresponding to the TEY and XET spectra in (a), (b), respectively. (e), (f) Sum spectra and cumulative sum-integral plots of the spectra in (a), (b), respectively.

to the projection of the sample magnetization vector onto the x-ray propagation vector. Considering the x-ray beam angle of 30° with respect to the surface plane, and 96% circular polarization of the x-ray beam, the effective m_l and m_s are estimated by $m_{l,s} = m_{l,s}(\text{measured})/(\cos 30^\circ \times 0.96)$.

Few-monolayer-thick Ni films can have a different n_h value than the bulk Ni or thicker Ni films due to the hybridization of Ni with the Cu(111) substrate [38]. To elucidate this effect, we calculated the electronic structure of a two-atomic-layer Ni film grown on a six-atomic-layer Cu(111) slab representing the substrate [Figs. 4(a) and 4(b)], using density functional theory (DFT) and DFT with spin-orbit coupling (DFT+SOC; Supplemental Material [39]; also see [40–44]). The calculations reveal hybridization between the Ni and Cu d states, accompanied by charge transfer from the Cu(111) substrate to the Ni overlayer. The Cu(111) substrate donates $0.51e$ to the Ni film in total, which contains 18 Ni atoms in the calculation. Notably, the transferred charge is localized mainly at the interfacial Ni layer, where Ni atoms gain $0.06e$ per atom. Thus we estimate the number of holes of the interfacial Ni atoms to be $n_h = 2-0.06 = 1.94$. In contrast, the Ni atoms at the topmost layer are almost unaffected and remain with $n_h \approx 2$.

The orbital and spin magnetic moments of the Ni film determined from the TEY and XET measurements are

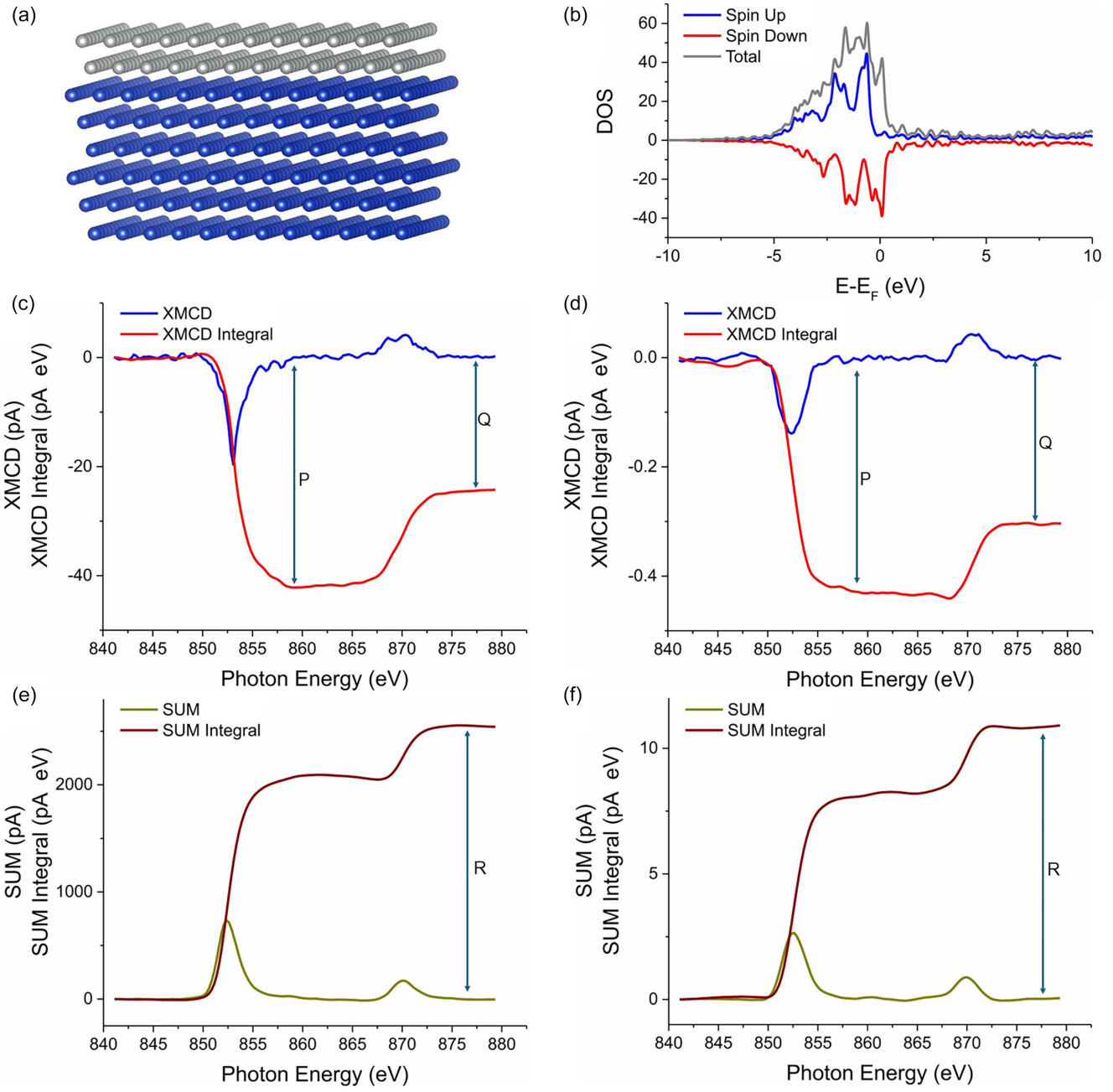

FIG. 4. (a) Geometry of the two-atomic-layer Ni on a Cu(111) slab used for the calculation. (b) Spin-up, spin-down, and total (spin-up + spin-down) density of states (DOS) of Ni calculated using the geometry in (a). (c), (d) XMCD and cumulative XMCD integral plots for TEY and XET modes at 22 K, respectively. (e), (f) Sum spectra and cumulative sum-integral plots of TEY and XET modes at 22 K, respectively.

summarized in Table I. For the TEY measurement, m_l and m_s at 90 K are found as $0.03 \pm 0.01\ \mu_B$ and $0.14 \pm 0.02\ \mu_B$, respectively. Here, an average value of $n_h = (2 + 1.94)/2 = 1.97$ is used. The measured m_l value agrees with the reported values in the literature (see the Supplemental Material [39]) [45]. Remarkably, for the XET measurements, the enhanced m_l and m_s are found as $0.09 \pm 0.01\ \mu_B$ and $0.34 \pm 0.02\ \mu_B$, respectively. Charge transfer predominantly occurs at the in-

TABLE I. Measured orbital and spin magnetic moments.

	TEY (90 K)	XET (90 K)	TEY (22 K)	XET (22 K)
m_l	$0.03 \pm 0.01\ \mu_B$	$0.09 \pm 0.01\ \mu_B$	$0.03 \pm 0.01\ \mu_B$	$0.09 \pm 0.01\ \mu_B$
m_s	$0.14 \pm 0.02\ \mu_B$	$0.34 \pm 0.02\ \mu_B$	$0.14 \pm 0.02\ \mu_B$	$0.31 \pm 0.02\ \mu_B$

terface, and its effect on the top-surface layer is assumed to be negligible. Thus we use $n_h = 2$ for the top-surface atomic layer. However, even if we use an averaged $n_h = 1.97$, the magnetic moments do not change significantly. The difference in magnetic moments between the XET and TEY modes is consistent with the expected preferential detection of the outermost surface atomic layer. Because TEY averages over the entire ∼2.5 ML film whereas x-ray-excited tunneling is strongly weighted toward the surface, the enhanced moments obtained from XET reflect increased sensitivity to low-coordination surface atoms whose magnetic properties can differ from those of the underlying film.

To check that the observed discrepancy in magnetic moments between XET and TEY modes is not related to the probe tip, XMCD measurements were performed in the far-field regime at 90 K. Here, the detector tip was positioned ∼10 nm above the surface to ensure that no tunneling occurred. Both the sample and tip channels were measured simultaneously using left- and right-circularly polarized x-rays. The results show the same orbital moment, $m_l = 0.03 \pm 0.01\ \mu_B$, and $m_s = 0.13 \pm 0.02\ \mu_B$ for the sample and the tip channel (see the Supplemental Material [39]). The similar magnetic moments measured at the tip and sample channels are because the tip in the far-field configuration captures a fraction of the photoejected electrons, which are not specific to the surface atomic layer. This measurement confirms that the higher magnetic moments observed in the XET mode are not attributable to the tip.

Next, to investigate the effect of temperature variation on the magnetic moments of the top-surface atomic layer, measurements are repeated on the same sample at a different temperature, 22 K [Figs. 4(c)–4(f)]. For the TEY mode, similar m_l and m_s values are found to be $0.03 \pm 0.01\ \mu_B$ and $0.14 \pm 0.02\ \mu_B$, respectively (Table I). They are similar to the values for the sample channel at 90 K. Similar values for m_L and m_S at 90 and 22 K substrate temperatures are expected because the sample magnetization is saturated below the Curie temperature of 150 K. For the XET measurements, the enhancements of m_l and m_s values are again found to be $0.09 \pm 0.01\ \mu_B$, and $0.31 \pm 0.02\ \mu_B$, respectively. These values are similar to those measured at 90 K, suggesting that the surface magnetization is also saturated.

Several theoretical studies have predicted enhanced spin and orbital magnetic moments due to narrowing of the *d* orbitals and reduced symmetry at the surface atomic layer [15–17]. These predictions are generally consistent with our findings; however, one caveat should be noted. The magnetic moments reported here were measured in a remanent state. In such measurements, the XMCD-derived values represent the projected remanent surface magnetic moment along the x-ray beam direction and, therefore, they are not necessarily equal to the fully saturated local Ni moment. Although we accounted for the angle between the x-ray beam and the surface plane, where the Ni magnetization direction is expected to lie, assigning a lateral angle between the x-ray beam and the Ni magnetization direction is not meaningful because the Ni film studied here is formed by coalescing two-dimensional (2D) islands. Multiple magnetic domains are therefore likely to be present in the Ni film, thereby significantly altering the measured magnetic moments. Nevertheless, the distinct magnetic moments measured for the topmost atomic layer and for the ensemble average of the Ni thin film clearly indicate that the XET can detect local magnetic moments in the top-surface atomic layer.

In summary, our findings establish an element-specific detection and quantification method for atomic-scale magnetism at the top-surface layer of a magnetic thin film using the x-ray-excited tunneling process. In electron tunneling, the current varies exponentially with the tip-sample distance; approximately an order of magnitude increase in current occurs when the distance is reduced to about 1 Å. Thus, it is extremely sensitive to the local electronic and magnetic properties of the outermost atomic layer. These findings establish that the x-ray-excited tunneling process using SX-STM is a powerful technique not only for detecting but also for quantifying magnetic moments at the atomic scale. This capability should enable measurements of local magnetic moments in individual magnetic nanoclusters and, potentially, even at the ultimate atomic limit.

We acknowledge financial support from the U.S. Department of Energy, Office of Science, Office of Basic Energy Sciences, Materials Science and Engineering Division. Work performed at the Center for Nanoscale Materials and Advanced Photon Source, both U.S. Department of Energy Office of Science User Facilities, was supported by the U.S. DOE, Office of Basic Energy Sciences, under Contract No. DE-AC02-06CH11357. We gratefully acknowledge the computing resources provided on Bebop, a high-performance computing cluster operated by the Laboratory Computing Resource Center at Argonne National Laboratory.

Data availability. There are no publicly available research data or software supporting this manuscript. Requests for further information or data should be sent to the authors.

S.W.H. and V.R. conceived and designed the project; S.P. and K.Z.L. prepared the samples; S.P., N.S., S.W., and V.R. performed the synchrotron experiments; S.P., N.S., and S.W.H. analyzed the data; D.R. prepared the detector "smart" tips; A.T.N. and A.T.L. performed DFT calculations; S.P. and S.W.H. wrote the paper. All the authors discussed the contents of the manuscript.

The authors declare no conflicts to disclose.

[1] F. Hellman *et al.*, Interface-induced phenomena in magnetism, Rev. Mod. Phys. **89**, 025006 (2017).

[2] C. A. F. Vaz, J. A. C. Bland, and G. Lauhoff, Magnetism in ultrathin film structures, Rep. Prog. Phys. **71**, 056501 (2008).

[3] S. Heinze, K. von Bergmann, M. Menzel, J. Brede, A. Kubetzka, R. Wiesendanger, G. Bihlmayer, and S. Blügel, Spontaneous atomic-scale magnetic skyrmion lattice in two dimensions, Nat. Phys. **7**, 713 (2011).

[4] M. Bode, M. Heide, K. von Bergmann, P. Ferriani, S. Heinze, G. Bihlmayer, A. Kubetzka, O. Pietzsch, S. Blugel, and R. Wiesendanger, Chiral magnetic order at surfaces driven by inversion asymmetry, Nature (London) **447**, 190 (2007).

[5] B. Issa, I. M. Obaidat, B. A. Albiss, and Y. Haik, Magnetic nanoparticles: Surface effects and properties related to biomedicine applications, Int. J. Mol. Sci. **14**, 21266 (2013).

[6] Q. A. Pankhurst, N. T. K. Thanh, S. K. Jones, and J. Dobson, Applications of magnetic nanoparticles in biomedicine, J. Phys. D: Appl. Phys. **36**, R167 (2003).

[7] I. Koh and L. Josephson, Magnetic nanoparticle sensors, Sensors **9**, 8130 (2009).

[8] P. Carra, B. T. Thole, M. Altarelli, and X. Wang, X-ray circular dichroism and local magnetic fields, Phys. Rev. Lett. **70**, 694 (1993).

[9] J. Stöhr, Exploring the microscopic origin of magnetic anisotropies with X-ray magnetic circular dichroism (XMCD) spectroscopy, J. Magn. Magn. Mater. **200**, 470 (1999).

[10] G. J. Omar, P. Gargiani, M. Valvidares, Z. S. Lim, S. Prakash, T. S. Suraj, A. Ghosh, S. T. Lim, J. Lourembam, and A. Ariando, Room temperature strong orbital moments in perpendicularly magnetized magnetic insulator, Adv. Funct. Mater. **35**, 2414188 (2025).

[11] F. Huang, M. T. Kief, G. J. Mankey, and R. F. Willis, Magnetism in the few-monolayers limit: A surface magneto-optic Kerr-effect study of the magnetic behavior of ultrathin films of Co, Ni, and Co-Ni alloys on Cu(100) and Cu(111), Phys. Rev. B **49**, 3962 (1994).

[12] S. Andrieu, T. Hauet, M. Gottwald, A. Rajanikanth, L. Calmels, A. M. Bataille, F. Montaigne, S. Mangin, E. Otero, P. Ohresser, P. Le Fèvre, F. Bertran, A. Resta, A. Vlad, A. Coati, and Y. Garreau, Co/Ni multilayers for spintronics: High spin polarization and tunable magnetic anisotropy, Phys. Rev. Mater. **2**, 064410 (2018).

[13] I. Galanakis, A. Debernardi, M. Alouani, and H. Dreyssé, Surface magnetism of 3*d* monolayers on a W(110) substrate probed by X-ray magnetic circular dichroism, Surf. Sci. **482–485**, 1030 (2001).

[14] V. Corradini, A. Ghirri, E. Garlatti, R. Biagi, V. De Renzi, U. del Pennino, V. Bellini, S. Carretta, P. Santini, G. Timco, R. E. P. Winpenny, and M. Affronte, Magnetic anisotropy of Cr_7Ni spin clusters on surfaces, Adv. Funct. Mater. **22**, 3706 (2012).

[15] O. Eriksson, A. M. Boring, R. C. Albers, G. W. Fernando, and B. R. Cooper, Spin and orbital contributions to surface magnetism in 3*d* elements, Phys. Rev. B **45**, 2868 (1992).

[16] I. M. L. Billas, A. Châtelain, and W. A. De Heer, Magnetism from the atom to the bulk in iron, cobalt, and nickel clusters, Science **265**, 1682 (1994).

[17] J. Bansmann, S. H. Baker, C. Binns, J. A. Blackman, J. P. Bucher, J. Dorantes-Dávila, V. Dupuis, L. Favre, D. Kechrakos, A. Kleibert, K. H. Meiwes-Broer, G. M. Pastor, A. Perez, O. Toulemonde, K. N. Trohidou, J. Tuaillon, and Y. Xie, Magnetic and structural properties of isolated and assembled clusters, Surf. Sci. Rep. **56**, 189 (2005).

[18] B. H. Frazer, B. Gilbert, B. R. Sonderegger, and G. De Stasio, The probing depth of total electron yield in the sub-keV range: TEY-XAS and X-PEEM, Surf. Sci. **537**, 161 (2003).

[19] R. Wiesendanger, Spin mapping at the nanoscale and atomic scale, Rev. Mod. Phys. **81**, 1495 (2009).

[20] M. Bode, Spin-polarized scanning tunnelling microscopy, Rep. Prog. Phys. **66**, 523 (2003).

[21] Y. Yayon, V. W. Brar, L. Senapati, S. C. Erwin, and M. F. Crommie, Observing spin polarization of individual magnetic adatoms, Phys. Rev. Lett. **99**, 067202 (2007).

[22] T. M. Ajayi, N. Shirato, T. Rojas, S. Wieghold, X. Cheng, K. Z. Latt, D. J. Trainer, N. K. Dandu, Y. Li, S. Premarathna, S. Sarkar, D. Rosenmann, Y. Liu, N. Kyritsakas, S. Wang, E. Masson, V. Rose, X. Li, A. T. Ngo, and S. W. Hla, Characterization of just one atom using synchrotron X-rays, Nature (London) **618**, 69 (2023).

[23] V. Rose, K. Wang, T. Chien, J. Hiller, D. Rosenmann, J. W. Freeland, C. Preissner, and S. W. Hla, Synchrotron X-ray scanning tunneling microscopy: Fingerprinting near to far field transitions on Cu(111) induced by synchrotron radiation, Adv. Funct. Mater. **23**, 2646 (2013).

[24] A. Saito, J. Maruyama, K. Manabe, K. Kitamoto, K. Takahashi, K. Takami, M. Yabashi, Y. Tanaka, D. Miwa, M. Ishii, Y. Takagi, M. Akai-Kasaya, S. Shin, T. Ishikawa, Y. Kuwaharaa, and M. Aonoa, Development of a scanning tunneling microscope for *in situ* experiments with a synchrotron radiation hard-X-ray microbeam, J. Synchrotron Rad. **13**, 216 (2013).

[25] T. Okuda, T. Eguchi, K. Akiyama, A. Harasawa, T. Kinoshita, Y. Hasegawa, M. Kawamori, Y. Haruyama, and S. Matsui, Nanoscale chemical imaging by scanning tunneling microscopy assisted by synchrotron radiation, Phys. Rev. Lett. **102**, 105503 (2009).

[26] N. Shirato, M. Cummings, H. Kersell, Y. Li, B. Stripe, D. Rosenmann, S. W. Hla, and V. Rose, Elemental fingerprinting of materials with sensitivity at the atomic limit, Nano Lett. **14**, 6499 (2014).

[27] H. Chang, N. Shirato, Y. Zhang, J. Hoffman, D. Rosenmann, J. W. Freeland, A. Bhattacharya, V. Rose, and S. W. Hla, X-ray magnetic circular dichroism and near-edge x-ray absorption fine structure of buried interfacial magnetism measured by using a scanning tunneling microscope tip, Appl. Phys. Lett. **113**, 061602 (2018).

[28] H. Kersell, N. Shirato, M. Cummings, H. Chang, D. Miller, D. Rosenmann, S. W. Hla, and V. Rose, Detecting element specific electrons from a single cobalt nanocluster with synchrotron X-ray scanning tunneling microscopy, Appl. Phys. Lett. **111**, 103102 (2017).

[29] S. Wieghold, N. Shirato, X. Cheng, K. Z. Latt, D. Trainer, R. Sottie, D. Rosenmann, E. Masson, V. Rose, and S. W. Hla, X-ray spectroscopy of a rare-earth molecular system measured at the single atom limit at room temperature, J. Phys. Chem. C **127**, 20064 (2023).

[30] S. Pons, P. Mallet, L. Magaud, and J. Y. Veuillen, Spontaneous evolution of the Ni/Cu(111) interface at 300 K, Surf. Sci. **511**, 449 (2002).

[31] K. Baberschke, The magnetism of nickel monolayers, Appl. Phys. A **62**, 417 (1996).

[32] P. Srivastava, F. Wilhelm, A. Ney, M. Farle, H. Wende, N. Haack, G. Ceballos, and K. Baberschke, Magnetic moments and Curie temperatures of Ni and Co thin films and coupled trilayers, Phys. Rev. B **58**, 5701 (1998).

[33] V. Rose, N. Shirato, M. Bartlein, A. Deriy, T. Ajayi, D. Rosenmann, S.-W. Hla, M. Fisher, and R. Reininger, XTIP–the world's first beamline dedicated to the synchrotron X-ray scanning tunneling microscopy technique, J. Synchrotron Rad. **27**, 836 (2020).

[34] Y. Ishii, Y. Yamasaki, Y. Kozuka, J. Lustikova, Y. Nii, Y. Onose, Y. Yokoyama, M. Mizumaki, J. Adachi, H. Nakao, T. Arima, and Y. Wakabayashi, Microscopic evaluation of spin and

orbital moment in ferromagnetic resonance, Sci. Rep. **14**, 15504 (2024).

[35] W. Kuch, X-ray magnetic circular dichroism for quantitative element-resolved magnetic microscopy, Phys. Scr. **2004**, 89 (2004).

[36] S. S. Dhesi, H. A. Dürr , G. van Der Laan, E. Dudzik, and N. B. Brookes, Electronic and magnetic structure of thin Ni films on Co/Cu(001), Phys. Rev. B **60**, 12852 (1999).

[37] C. T. Chen, Y. U. Idzerda, H.-J. Lin, N. V. Smith, G. Meigs, E. Chaban, G. H. Ho, E. Pellegrin, and F. Sette, Experimental confirmation of the X-ray magnetic circular dichroism sum rules for iron and cobalt, Phys. Rev. Lett. **75**, 152 (1995).

[38] A. Ernst, G. van der Laan, W. M. Temmerman, S. S. Dhesi, and Z. Szotek, Contesting results for magnetic moments in nickel thin films, Phys. Rev. B **62**, 9543 (2000).

[39] See Supplemental Material at http://link.aps.org/supplemental/10.1103/2fdk-tmsx for DFT calculation procedure, additional experimental results, and supporting tables, which include Refs. [40–44].

[40] G. Kresse and J. Hafner, *Ab initio* molecular dynamics for liquid-metals, Phys. Rev. B **47**, 558 (1993).

[41] G. Kresse and J. Furthmuller, Efficient iterative schemes for *ab initio* total-energy calculations using a plane-wave basis set, Phys. Rev. B **54**, 11169 (1996).

[42] P. E. Blochl, Projector augmented-wave method, Phys. Rev. B **50**, 17953 (1994).

[43] G. Kresse and D. Joubert, From ultrasoft pseudopotentials to the projector augmented-wave method, Phys. Rev. B **59**, 1758 (1999).

[44] J. P. Perdew, K. Burke, and M. Ernzerhof, Generalized gradient approximation made simple, Phys. Rev. Lett. **77**, 3865 (1996).

[45] C. Boeglin, S. Stanescu, S. Cherifi, J. P. Deville, P. Ohresser, A. Barbier, and N. B. Brookes, High dipolar magnetic moment observed on Ni/Cu(111) nanostructures by magnetic circular X-ray dichroism, Surf. Sci. **507–510**, 522 (2002).